Journal of Power Sources 662 (2026) 238813

Contents lists available at ScienceDirect

Journal of Power Sources

journal homepage: www.elsevier.com/locate/jpowsour

Achieving high energy density with all pseudocapacitive asymmetric materials as energy storage device: Metallic ruthenium confined in MOF-derived N-doped porous carbon as positive and free-standing Ti_3C_2 film as negative electrode

Elangovan Sivasurya [a,1], Mari Elancheziyan [b,1], Francis Ashamary [a,1], Ganesan Maheswari [a,1], Atchudan Raji [c,d,1], Mohamed Gamal Mohamed [e,f,*,1], Annamalai Padmanaban [g,h], Keehoon Won [b], Pramod K. Kalambate [i,**], Shiao-Wei Kuo [e,j,***], Devaraj Manoj [a,****]

[a] *Department of Chemistry, Centre for Material Chemistry, Karpagam Academy of Higher Education, Coimbatore, 641021, India*
[b] *Department of Chemical and Biochemical Engineering, College of Engineering, Dongguk University-Seoul, 30 Pildong-ro 1-gil, Jung-gu, Seoul, 04620, Republic of Korea*
[c] *Department of Chemistry, Saveetha School of Engineering, Saveetha Institute of Medical and Technical Sciences, Chennai, 602105, Tamil Nadu, India*
[d] *School of Chemical Engineering, Yeungnam University, Gyeongsan, 38541, Republic of Korea*
[e] *Department of Materials and Optoelectronic Science, Center for Functional Polymers and Supramolecular Materials, National Sun Yat-Sen University, Kaohsiung, 804, Taiwan*
[f] *Department of Chemistry, Faculty of Science, Assiut University, Assiut, 71515, Egypt*
[g] *Facultad de Ingenieria, Universidad Catolica de la Santisima Concepcion, Concepcion, 4090541, Chile*
[h] *Department of Physiology, Saveetha Institute of Medical and Technical Sciences, Chennai, 600077, India*
[i] *Department of Chemistry & Waterloo Institute for Nanotechnology, University of Waterloo, Waterloo, Ontario N2L 3G1, Canada*
[j] *Department of Medicinal and Applied Chemistry, Kaohsiung Medical University, Kaohsiung, 807, Taiwan*

HIGHLIGHTS

- A new class of Ru@N doped C positive electrode was prepared from pillared Ru-MOF.
- Ru@N-doped C exhibited a higher specific capacitance (211.1 F g^{-1}) than reported RuO_2.
- All pseudocapacitive device was assembled using Ti_3C_2 film and Ru@N doped C.
- ASC device demonstrates high power (1294 W kg^{-1}) and energy density (60.7 Wh kg^{-1}).
- Ti_3C_2//Ru@N doped C device achieved high capacitive retention.

ARTICLE INFO

Keywords:
Metallic Ru
N-doped carbon
MXene
Free-standing flexible film
Pseudocapacitive electrodes

ABSTRACT

Herein, we report for the first time the transformation of non-conductive ruthenium (Ru)-based metal-organic frameworks (Ru-MOFs) into MOF-derived metallic Ru encapsulated by a nitrogen-doped graphitic carbon matrix (Ru@N-doped C), forming a nano-heterostructured interface. This unique feature offered by Ru@N-doped C facilitates the generation of abundant redox-active sites (Ru) while promoting efficient ion transport through well-defined diffusion channels (N-doped C) in sulfuric acid (H_2SO_4, 1 M). The resultant Ru@N-doped C electrode exhibits a faradaic (non-diffusion-limited) charge storage mechanism, and the calculated specific capacitance (211.1 F g^{-1} at 1 A g^{-1}) outperforms other pristine ruthenium dioxide (RuO_2)-based electrodes. The

---

* Corresponding authors. Department of Materials and Optoelectronic Science, Center for Functional Polymers and Supramolecular Materials, National Sun Yat-Sen University, Kaohsiung, 804, Taiwan.

** Corresponding author.

*** Corresponding authors. Department of Medicinal and Applied Chemistry, Kaohsiung Medical University, Kaohsiung, 807, Taiwan.

**** Corresponding author.

E-mail addresses: mgamal.eldin34@gmail.com, mgamal.eldin12@aun.edu.eg (M.G. Mohamed), pramodkalambate1@gmail.com (P.K. Kalambate), kuosw@faculty.nsysu.edu.tw (Shiao-Wei Kuo), manojdvrj@gmail.com, manoj.devaraj@kahedu.edu.in (D. Manoj).

[1] These authors contributed equally.

https://doi.org/10.1016/j.jpowsour.2025.238813
Received 5 June 2025; Received in revised form 17 October 2025; Accepted 7 November 2025

synergistic integration of highly conductive N-doped carbon with metallic Ru enhances both redox activity and ion diffusion kinetics, while maintaining excellent rate capability. When Ru@N-doped C (positive electrode) is integrated with pseudocapacitive Ti_3C_2 MXene free-standing film (negative electrode), it exhibits all pseudocapacitive asymmetric device configurations and delivers superior specific capacitance (194.3 F g^{-1} at 1 A g^{-1}), accompanied by faradaic efficiency (90 %) and capacitive retention (109 %). The asymmetric (ASC) device demonstrates high energy density (60.7 Wh kg^{-1}) and power density of 1294 W kg^{-1}, which outperforms other reported RuO_2-based devices.

1. Introduction

In today's energy-driven world, the demand for compact, high-performance energy storage devices is rapidly increasing [1–6]. Pseudocapacitors have emerged as promising candidates due to their high energy density and rapid charge–discharge capability, making them ideal for flexible and wearable electronics [7–11]. Transition metal oxides [Co_3O_4, V_2O_5, NiO, and MnO_2] are widely studied electrodes to enhance specific capacitance through redox reactions and ion intercalation [12–15]. However, Ruthenium dioxide (RuO_2, which belongs to the platinum group) is unique when compared to other transition metal oxides due to its multivalent state enables a surface redox transfer process [16]. RuO_2 was considered as the first electrode material, which undergoes a reversible redox reaction at the near electrode surface called pseudocapacitance, was reported in early 1971 [17]. Further studies revealed that hydrous RuO_2 (RuO_2. xH_2O) is reported with high capacity and rate capability, which are greatly dependent on the electrolyte and surface chemistry of the material, resulting in excellent theoretical capacitance (>2000 F g^{-1}). Although both hydrous and anhydrous RuO_2 exhibited pseudocapacitive behavior, they are limited by severe aggregation and are difficult for penetration of electrolyte ions to activate electroactive sites, and thus, this diminishes the faradaic (non-diffusion) reaction, resulting in low capacitance. Additionally, RuO_2 electrodes suffer from poor rate capability at high charge/discharge rates due to limited electrical conductivity and lesser cyclic stability [18]. Moreover, the fabrication of various reported hybrid asymmetric devices is configured mainly by combining RuO_2 (positive electrode) and carbon (negative electrode), whereas the practical applications are limited by high cost and low active surface area of RuO_2. Recent efforts focus on all-pseudocapacitive systems, where both electrodes contribute to redox storage, offering a promising path toward next-generation high-energy devices [19].

Generally, the selection of pseudocapacitive materials and current collectors is critical, as it directly influences charge–discharge efficiency, which can influence the device performance with long-term stability [20]. MOFs represent a suitable class of electrode materials for energy storage applications, owing to their excellent electrochemical stability [21]. This is primarily attributed to the formation of strong coordination bonds between metal nodes and organic linkers, which not only offer abundant pseudocapacitive sites but also contribute to a high surface area. Many studies have demonstrated that pre-synthesized MOFs can be transformed into porous carbon materials through controlled thermal treatment at specific temperatures. The resulting MOF-derived carbon features high porosity, large surface area, and improved electrical conductivity, which together facilitate ion accessibility towards the active sites and promote electron transfer [22]. Among the diverse MOF structures, Ru-MOFs have distinguished themselves from other MOF analogs and derivatives due to their superior pseudocapacitive charge storage capacity and remarkable electrochemical stability, particularly in acidic media. Although the use of bulk RuO_2 in combination with carbon-based negative electrodes to fabricate ASCs has been widely reported in the literature, emerging research on MOF-derived materials are expected to deliver promising avenues for energy storage performance [23,24].

Carbon-based materials are widely regarded as ideal negative materials for ASCs due to their excellent electronic conductivity, high surface area, mechanical stability, cost-effectiveness, abundance, and environmentally friendly nature [25,26]. Widely used carbonaceous materials, including carbon nanotubes (CNTs), activated carbon (AC), and graphene, have been extensively studied. However, these materials often exhibit relatively low specific capacitance (Cs), which has driven the exploration of alternative materials. To overcome these limitations, researchers have investigated non-noble transition metal oxides, nitrides, and carbides. Among these, MXenes (Titanium carbide, Ti_3C_2), a group of 2D materials composed of metal carbides and nitrides, have emerged as promising candidates in energy storage devices [27,28]. Their strong pseudocapacitive properties, highly reversible redox behavior in acidic media, and excellent metallic conductivity make them particularly attractive for advanced asymmetric devices [29]. In particular, the inherent high metallic conductivity offered by free-standing MXene films has demonstrated exceptionally high specific capacitance and excellent cyclic stability. These features enable efficient charge transfer between the electrode and electrolyte, underscoring the potential of $Ti_3C_2T_x$ as a highly promising negative electrode for next-generation supercapacitors [30].

In the present work, we proposed a novel strategy to fabricate an ASC device based on all pseudocapacitive electrode materials, which combines a freestanding Ti_3C_2 film (as negative electrode) with a metallic Ru@N-doped C (as positive electrode) on graphite foil, a configuration that has not been reported to date. The Ru-MOF was synthesized using 1,2,4,5-benzene tetracarboxylic acid as the linker and a pre-synthesized organic ligand namely 2,6-di(1H-imidazole-2-yl)pyridine [2,6-DIPy] under hydrothermal conditions, followed by thermal annealing in presence of melamine to form Ru@N-doped C. During the annealing process, melamine facilitated the formation of a hierarchically interconnected N-doped graphitic carbon layer, which effectively preserved the metallic nature of Ru against oxidation. The freestanding Ti_3C_2 film was prepared via etching, delamination, and exfoliation of the Ti_3AlC_2 (MAX) phase using a LiF/HCl mixture, commonly referred to as the MILD method. When an asymmetric device is fabricated, the operating potential of the assembled freestanding Ti_3C_2 film//Ru@N-doped C-based ASC device was successfully extended up to 1.5 V by utilizing a faradaic non-diffusion process without any oxygen evolution. This expanded operating voltage significantly enhanced the energy density of all asymmetric pseudocapacitive electrodes without compromising their power density.

2. Experimental section

2.1. Synthesis of pillared Ru-MOF

Pillared Ru-MOF was synthesized through a one-pot hydrothermal reaction, which involves 2,6-di(1H-imidazole-yl)pyridine [2,6-DIPy] as organic ligand, 1,2,4,5-benzene tetracarboxylic acid (organic linker), and $RuCl_3$ as a metal precursor. In a typical synthesis, 0.25 mmol of 1,2,4,5-benzene tetracarboxylic acid and 0.25 mmol of 2,6-DIPy were dissolved in DMF to form solution A. 0.2 mmol $RuCl_3 \cdot xH_2O$ was added to 15 mL of water to form solution B. For the formation of MOF, solution B was added dropwise into solution A and stirred continuously at 25 °C for 30 min. The resultant homogeneous mixture was transferred into a Teflon-lined stainless-steel autoclave, heated at 120 °C for 72 h, and allowed to reach ambient temperature (25 °C). The obtained products were filtered, washed with ethanol and water, dried under vacuum at 60 °C, and named as pillared Ru-MOF.

2.2. Synthesis of Ru-MOF derived N-doped carbon (Ru@N-doped C)

About 100 mg of pre-synthesized Ru-MOF was subjected to grinding with a hand pestle in the presence of 0.9 g) melamine (N-doped C source) for 30 min to obtain a homogenous mixture. The fine powders were transferred into an alumina boat and kept in a tubular furnace, subjected to annealing (500 °C) for 1 h and then ramped to 900 °C and maintained at the same temperature for 2h, with a continuous flow of Ar/H_2 (90:10) atmosphere. After the annealing process, the samples were cooled to ambient temperature and named as Ru@N doped C.

2.3. Preparation of freestanding Ti_3C_2 film

The preparation of single-layered Ti_3C_2 nanosheets involves the etching of the MAX (Ti_3AlC_2) phase and followed by delamination of multi-layered $Ti_3C_2T_x$ (m-$Ti_3C_2T_x$) via the MILD method as previously reported [31]. Typically, Ti_3AlC_2 (1 g) powder was added to the etchant solution containing LiF and HCl and stirred at 0 °C for 1 h. The reaction temperature increased to 35 °C by transferring into an oil bath, and the mixture was stirred continuously for 48 h. The reaction mixture was transferred into a centrifuge tube (50 mL) and centrifuged at 3500 rpm for 5 min until the pH of the supernatant became 6. The supernatant became dark green at pH > 6.5 to obtain m-$Ti_3C_2T_x$.

To delaminate m-$Ti_3C_2T_x$, a freshly prepared LiCl solution was added and allowed to intercalate between the multi-layered Ti_3C_2 nanosheets and subjected to stirring at 400 rpm for 6 h. After completion, the homogenous mixture was separated by centrifuge at 3500 rpm for 5 min, and the collected sediment was then redispersed in 20 mL of DI water, and this process was repeated until the observation of dark supernatant. The greenish-black supernatant was collected in an Ar-sealed bottle, and the delamination process was continued by redispersing the swollen sediment with 10 mL of water to obtain a Ti_3C_2 solution of about 100 mL. To obtain a freestanding Ti_3C_2 film, the dark suspension was transferred into vacuum-assisted filtration by placing a PVDF membrane filter between the setups. After slow filtration of about 3 h, the Ti_3C_2 supported on the PVDF membrane filter was placed at 60 °C under vacuum, and the freestanding Ti_3C_2 film was peeled off from the membrane filter.

3. Results and discussion

3.1. Characterization of Ru-MOF and Ru@N-doped carbon

In this work, a two-step synthesis process was employed, as illustrated in Fig. 1. In the first step (stage 1), a pillared Ru-MOF was synthesized via a one-pot hydrothermal reaction, which involved 2,6-DIPy as the organic ligand (serving as the pillaring agent), 1,2,4,5-benzene tetracarboxylic acid as the linker, and $RuCl_3$ as the metal precursor. The reaction was carried out at 120 °C for 3 days. In the second step (stage 2), the as-synthesized pillared Ru-MOF was mixed with melamine, serving as the nitrogen-doped carbon source, and subsequently annealed at 900 °C for 2 h under Ar/H_2 atmosphere to obtain Ru@N-doped C. During the annealing process, the intrinsically insulating Ru-MOF was transformed into a metallic Ru surrounded by N-doped carbon layer at the heterointerface, which can protect Ru from oxidation, and thus, conductivity can be retained. The structural and morphological changes at the heterointerface before (Ru-MOF) and after the melamine treatment (Ru@N-doped C) were further investigated through the following detailed characterizations. To elucidate the formation of the carbon layer, the as-prepared Ru-MOF (without annealing) and the results were systematically compared with those of Ru@N-doped C [Fig. 2 (a)]. The synthesis of Ru-MOF involves the incorporation of organic ligands and linkers, leading to the formation of broad diffraction peaks in the absence of post-synthetic thermal treatment. The powder XRD patterns of both Ru-MOF (without annealing) are visualized in the form of broad humps without any sharp peaks, which are mainly relevant to the diffuse scattering behavior and the resultant Ru-MOF without annealing, and therefore, it existed in the form of amorphous nature. Upon annealing, a noticeable broadening of diffraction peaks is observed at Ru@N-doped C, suggesting the resulting material is obtained as a nanocrystalline form. Distinct, sharp diffraction peaks appearing at 38.44°, 43.99°, 58.52°, 69.38°, and 78.50° correspond to the (100), (101), (102), (110), and (103) planes, respectively, of the hexagonal close-packed (hcp) crystalline structure of metallic Ru, consistent with the standard ICDD reference (No. 002–1258) [32,33]. These peak positions align well with previously reported values for hcp Ru, further confirming the successful formation of metallic Ru. In addition to these features, the XRD pattern of Ru@N-doped C displays new broad and intense peaks centered around 27.36° is attributed to the (002) lattice plane of amorphous carbon [34]. This observation indicates the presence of a carbonaceous layer with an amorphous skeletal structure formed during high-temperature annealing. Moreover, a slight shift in diffraction peaks toward lower angles suggests interlayer distortion,

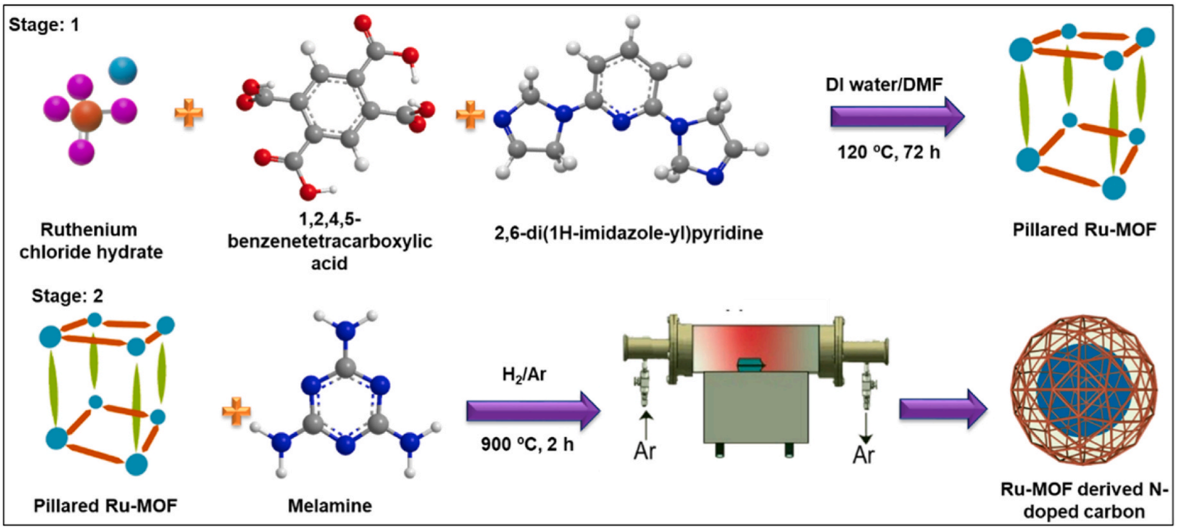

Fig. 1. Schematic representation of stage-wise preparation of Ru-MOF-derived N-doped porous carbon (Ru@N-doped C).

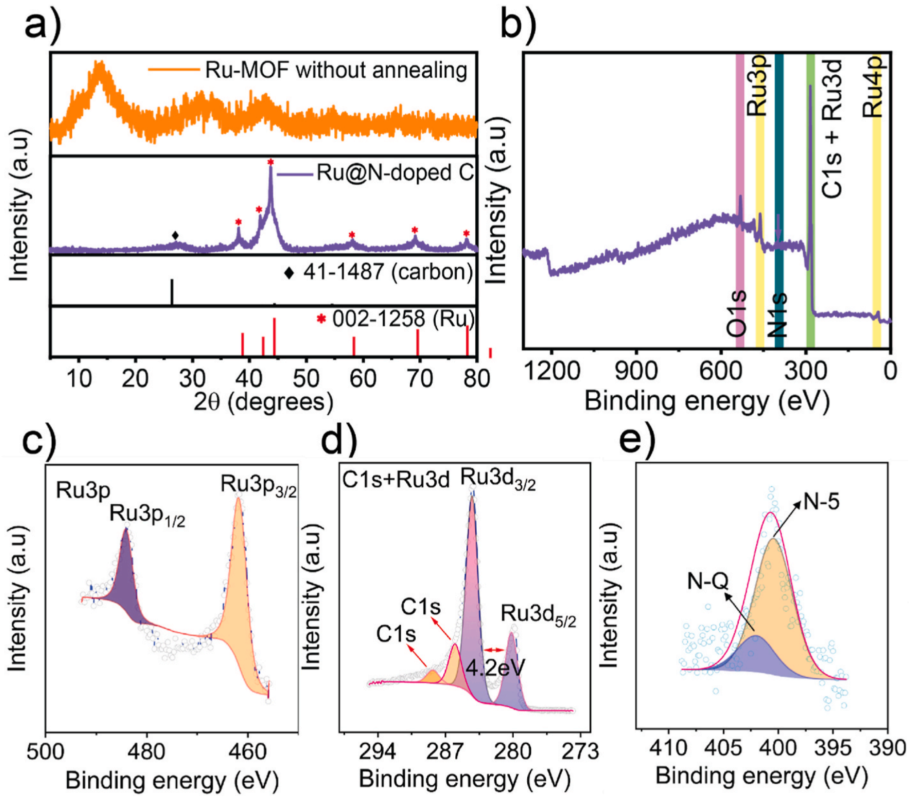

Fig. 2. (a) XRD spectra of Ru-MOF and Ru@N-doped C. (b) XPS spectrum survey spectrum of Ru@N-doped C (c) Ru 3p, (d) C 1s + Ru 3d, and (e) N 1s.

likely arising from tensile strain within the Ru lattice induced by the thermal treatment. The average crystallite size, calculated using the Scherrer equation for the dominant (101) peak of Ru, was found to be approximately 3.44 nm.

The formation of N-doped carbon during annealing leads to the coexistence of graphitic and amorphous carbon phases. This structural heterogeneity, combined with heteroatom (N) doping, is expected to improve the electrical conductivity of the composite material. To investigate the elemental composition and oxidation state of metallic Ru encapsulated within the N-doped carbon matrix, XPS analysis was carried out. As shown in the survey spectrum [Fig. 2(b)], the Ru@N-doped C composite consists exclusively of Ru, C, N, and O elements, indicating the obtained material is free from impurities. Detailed analysis of the Ru 3p core level region [Fig. 2(c)], deconvoluted using a Shirley background between 495 and 455 eV, reveals a pair of well-defined peaks located at 461.7 eV and 484.2 eV [35,36]. These peaks are assigned to Ru $3p_{3/2}$ and Ru $3p_{1/2}$ of metallic Ru (Ru^0), respectively. Absence of peaks associated with oxidized Ru species, along with the observed spin–orbit splitting of 22.5 eV, further confirms the presence of metallic Ru within the Ru@N-doped C matrix. In the HR-XPS narrow scanning region between 275 and 295 eV, the overlapping signals of C 1s and Ru 3d were simultaneously deconvoluted [Fig. 2(d)]. The C 1s spectrum shows two distinct peaks at 286.1 eV and 288.3 eV, which correspond to $-C \equiv N$ and -C=N bonds, respectively, indicative of nitrogen incorporation into the carbon framework. This region overlaps with the Ru 3d signals, collectively designated as the Ru 3d + C 1s region. The deconvoluted Ru 3d spectra exhibit two spin-orbit peaks at 280.2 eV ($3d_{5/2}$) and 284.4 eV ($3d_{3/2}$), which are consistent with metallic Ru (spin–orbit splitting of 4.2 eV), confirming its preserved oxidation state during the post-annealing process [37]. According to Fig. 2(e)–N 1s high-resolution XPS spectra were deconvoluted, and a closer observation of the N 1s peak is splitting into two binding energy positions located at 400. 7 and 402.1 eV, which corresponds to the existence of pyrrolic (N-5) and graphitic-N (N-Q), respectively. These features strongly revealed the formation of an N-doped graphitic C layer protecting the metallic Ru and together to form Ru@N-doped C. The O 1s spectrum [Fig. S1] exhibits broad features, which can be attributed to the presence of multiple oxygen species. A prominent peak centered at 532.8 eV is primarily ascribed to chemisorbed water molecules, whereas a shoulder at a lower binding energy (530.5 eV) corresponds to surface oxide species, such as RuO_2, or potentially metallic Ru with surface-bound oxygen. However, the formation of oxygen cannot be neglected, and it can be formed when transferring samples into the vacuum chamber. The morphology of the synthesized samples, namely Ru-MOF (without annealing) and Ru@N-doped C, was investigated using SEM and TEM analyses. As seen in the SEM image, the Ru-MOF exhibits an agglomeration of particles that are fused to form an elongated pillar-like morphology [Fig. 3(a)]. This might be due to the reaction conditions carried out for 3 days, which favor the slow agglomeration of nanoparticles into the pillared structure. However, after annealing the Ru-MOF in the presence of melamine at 900 °C, the morphology of the Ru@N-doped C undergoes a substantial transformation, with no observable particles. This transformation is visualized as a skeleton structure with a porous network on its surface, formed during the carbonization process [Fig. 3(c)] [38]. Furthermore, analysis of Ru-MOF and Ru@N-doped C at the atomic level using elemental mapping reveals that the corresponding elemental distributions of Ru, C, and N atoms are uniformly distributed in the prepared samples [Fig. 3(b) and (d)]. During the annealing process, melamine and the organic ligands in Ru-MOF first condense to form a carbon skeleton and a layered graphitic carbon nitride structure at 500 °C. The morphology of the wrinkled skeleton structure originates from the morphology of graphitic carbon nitride. Subsequently, the N-doped C is produced from the carbonization of graphitic C_3N_4 at 900 °C.

Furthermore, the formation of a heterojunction of the N-graphitic carbon layer in Ru@N-doped C was confirmed by TEM analysis. All the Ru particles were uniformly distributed on the surface of Ru@N-doped C and had an average size of 3–4 nm [Fig. 4(a) and (b)]. A closer

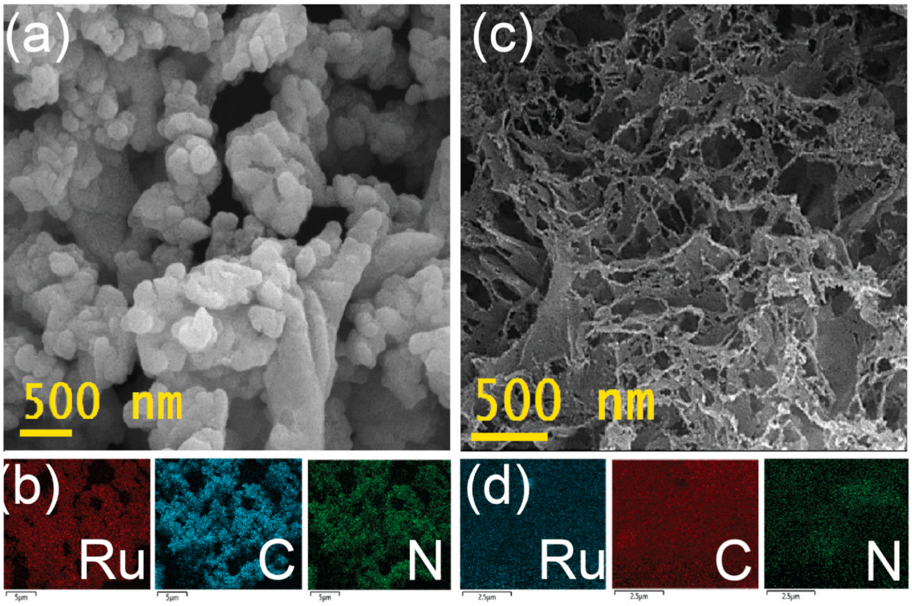

Fig. 3. SEM image of (a) Ru-MOF and (c) Ru@N-doped C. Elemental mapping of (b) Ru-MOF and (d) Ru@N doped C.

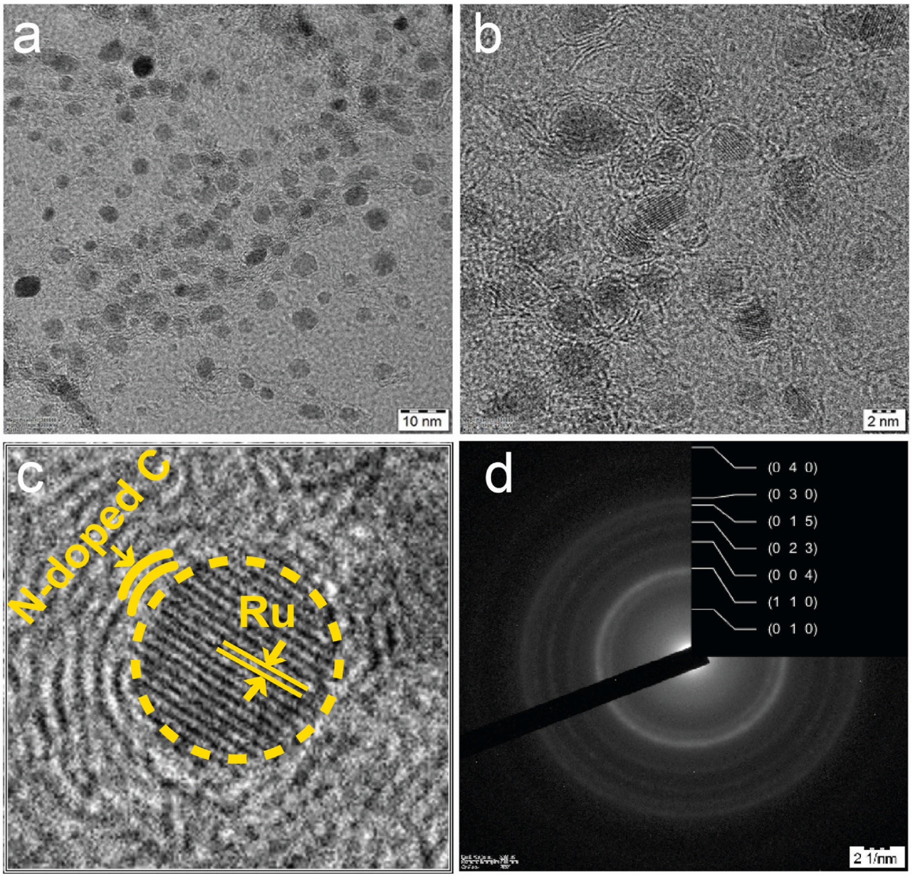

Fig. 4. (a and b) TEM image of Ru@N-doped C (c) High-resolution TEM image of Ru@N-doped C. (d) The corresponding SAED pattern.

observation of the TEM image revealed that individual dark spots are observed bounded by the carbon layer, indicating the formation of Ru particles without any aggregation was observed for Ru@N-doped C. A magnified view of the HRTEM image [Fig. 4(c)] reveals Ru NPs with well-defined lattice fringes and a calculated d-spacing of 0.0234 nm, corresponding to the (111) Ru crystalline plane. Three to four layers of carbon shells with a calculated lattice spacing of 0.34 nm encapsulate the metallic Ru, revealing the formation of a graphitic carbon skeleton structure. In addition, the selected area electron diffraction (SAED) pattern exemplifies the polycrystalline nature of the Ru@N-doped C, showing well-defined diffraction rings corresponding to the respective crystalline facets, as mentioned in Fig. 4(d). To further verify the formation of metallic Ru and the formation of N-doped C layer after annealing of Ru-MOF in the presence of melamine was evaluated using thermogravimetric (TGA) and FT-IR analyses. TGA analyses of Ru-MOF and Ru@N-doped C [Fig. S2] were conducted from room temperature to 900 °C under a nitrogen atmosphere. The TGA curve of Ru-MOF (orange line) shows an initial weight loss of ~7 % below 100 °C, attributed to the evaporation of water molecules. A major weight loss of ~50 % occurs between 200 and 550 °C due to the decomposition of coordination water and the breakdown of organic ligands (1,2,4,5-benzene tetracarboxylic acid and 2,6-DIPy) into carbonaceous materials, with complete degradation around 550 °C. Beyond this temperature, a gradual weight loss is observed, leaving 29.7 % of the initial mass (1.674 mg from 2.38 mg), indicating the presence of Ru as the residue. In the case of Ru@N-doped C, an initial ~10 % weight loss below 50 °C corresponds to the removal of adsorbed moisture, followed by a second loss near 250 °C, assigned to the decomposition of surface functional groups. From 250 to 900 °C, only slight weight changes are observed, resulting in 68.7 % residue at 900 °C, attributed to metallic Ru. These results confirm the successful incorporation of Ru in both Ru-MOF and Ru@N-doped C. Fig. S3 compares the FT-IR spectra of Ru-MOF and Ru@N-doped C, recorded in ATR mode within the wavenumber range of 4000–500 cm^{-1}. For Ru-MOF, strong absorption bands between ~1700 and 800 cm^{-1} indicate the presence of the organic linker 1,2,4,5-benzene tetracarboxylic acid and the organic ligand 2,6-DIPy. The characteristic peaks at 1608 and 1503 cm^{-1} are assigned to C=C and C=N stretching vibrations of pyridine, confirming the presence of 22,6-DIPy. A broad band at 1281 and 1114 cm^{-1} corresponds to C–H in-plane bending, while the strong peak at 1074 cm^{-1} is attributed to C–C stretching of 1,2,4,5-benzene tetracarboxylic acid. In addition, the weak band at 1390 cm^{-1}, associated with C–O stretching, suggests strong coordination between Ru and the organic linker. In contrast, the FT-IR spectrum of Ru@N-doped C shows the disappearance of the C–C, C–O, and C=N peaks, indicating the dissociation of both the ligand and the linker upon thermal annealing. Furthermore, the Ru-related vibration observed at ~540 cm^{-1} in Ru-MOF shifts to 551 cm^{-1} in Ru@N-doped C, confirming the presence of Ru in the carbonized framework.

3.2. *Electrochemical performance of Ru@N-doped C as positive electrode*

Since the electrochemical performance of each modified electrode plays a crucial role in determining the efficiency of ASCs, it highlights the importance of assessing and optimizing the pseudocapacitive behavior of both positive as well as negative electrodes [31]. Moreover, each electrochemical test was conducted in a standard three-electrode setup in the presence of a 1 M H_2SO_4 aqueous solution to evaluate the pseudocapacitive ability. The choice of H_2SO_4 solution as the electrolyte is crucial, as its outstanding ion conductivity and the presence of the smallest cation facilitate high electrochemical performance. Initially,

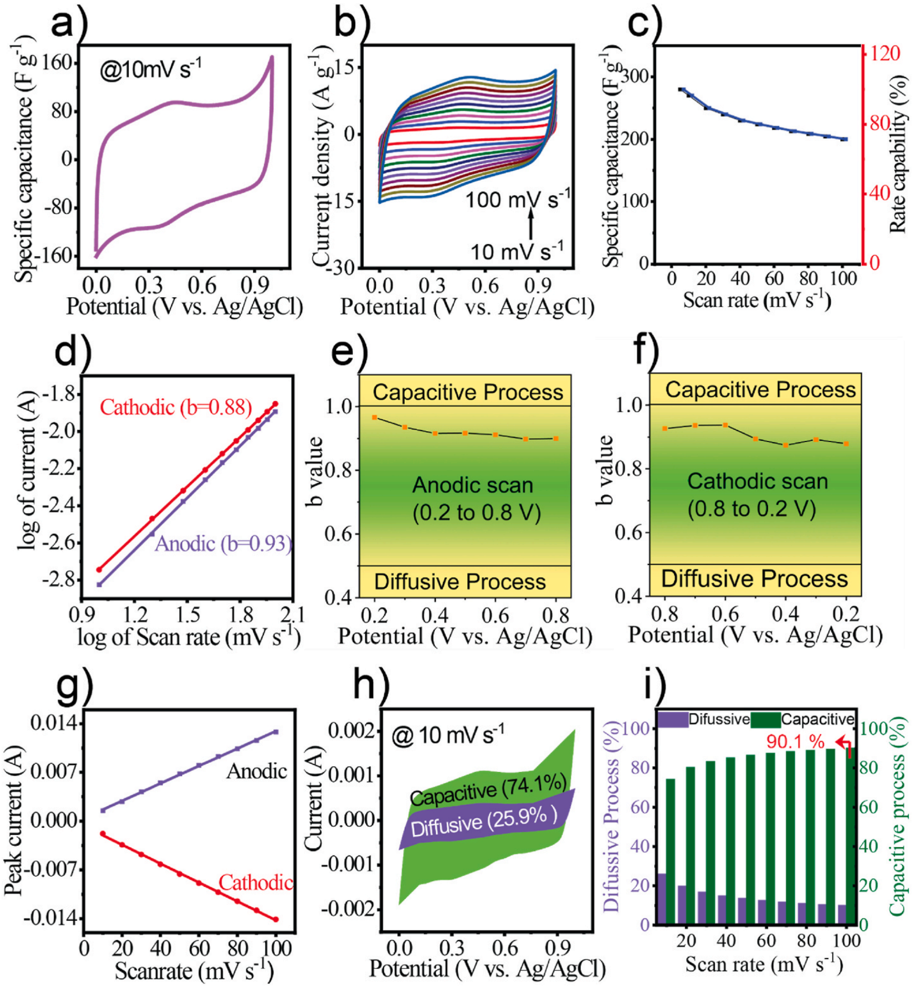

Fig. 5. (a) The CV curve for Ru@N-doped C in 1 M H_2SO_4 at 10 mV s^{-1} using a three-electrode cell configuration. (b) CV curves of Ru@N-doped C performed at different scan rates from 10 mV s^{-1} to 100 mV s^{-1}. (c) Specific capacitance for Ru@N-doped C derived from the CV plots at different scan rates. (d) Log current vs log scan rate of Ru@N-doped C. (e and f) The calculation of b values for Ru@N-doped C in the anodic and cathodic process at different potentials. (g) The plot of scan rate vs peak current for the Ru@N-doped C. (h) Capacitive and diffusive contribution at 10 mV s^{-1}. (i) Ratio of capacitive and diffusive-controlled processes at different scan rates.

the electrochemical behavior of Ru@N-doped C as the positive electrode was investigated in a three-electrode configuration using cyclic voltammetry (CV), electrochemical impedance spectroscopy (EIS), and galvanostatic charge-discharge (GCD), respectively. A half-cell was fabricated with the Ru@N-doped C and Super P along with PVDF as a binder in the ratio of (8:1:1) with a few drops of NMP as a solvent. The prepared slurry was carefully coated using the doctor-blade method onto a well-cleaned activated graphite foil, which acted as a current collector. More details of electrode preparation are explained in the experimental section. Electrochemical behavior of Ru@N-doped C was studied from the CV profile in 1 M H_2SO_4 aqueous solution at 10 mV s^{-1} within the potential window from 0 to 1.0 V [Fig. 5(a)]. The CV response shows a slightly distorted rectangular CV pattern contributed by the N-doped carbon layer, whereas the observation of a redox peak located at Epa = +0.40 V and Epc = +0.35 V signifies the electronic transition process of Ru^{3+}/Ru^{2+}, demonstrating their pseudocapacitive behavior [39–41]. The observation of a distorted CV curve is mainly due to the presence of N-doped porous carbon. Under thermal annealing in the presence of melamine, it induces the formation of N doping on edge sites of the carbon matrix, and leads to various N-configurations, namely pyrrole N (N-5) and quaternary N (N-Q), respectively [42].

As a result, the presence of heteroatom dopant (N) in Ru@N-doped C enables pseudocapacitive reaction with electrolyte ions, and the manipulated local electronic structures allow for enhanced binding with ions. The significant difference in the electronegativity of N (Pauling scale: 3.04) and C (Pauling scale: 2.55) causes the polarization between nitrogen dopants and their adjacent carbon atoms, and the changed charge distribution enhances the number of hydrophilic polar sites, which gives rise to the enhanced wettability in aqueous electrolyte medium [43]. Moreover, nitrogen dopants could induce high electron density of the local carbon atoms in the graphitic structure, which contributes to surface pseudocapacitance by reversible chemical adsorption/desorption of ions in electrolyte solution. Those electrochemically active N dopant sites are involved in the faradaic charge transfer and contribute to pseudocapacitance. In addition, the Ru@N-doped C demonstrated capacitive behavior, as shown by its large area enclosed in the CV profile. Additionally, there is a small potential difference between the anodic and cathodic peaks, which is ascribed to the fast electron transfer kinetics, ensuring the high-capacity characteristics of the Ru@N-doped C electrode. Further, the charge transfer mechanism, rate capability, and detailed capacitive properties of Ru@N-doped C were explored by increasing scan rates from 10 to 100 mV s^{-1} [Fig. 5(b)]. Despite the increase in scan rates, the CV profile retained both cathodic and anodic peaks even at a higher scan rate at 100 mV s^{-1}, indicating the Ru@N-doped C electrode exhibited excellent rate capability. In addition, while increasing the scan rate from 10 to 100 mV s^{-1}, it is observed that the oxidation and reduction peak currents slightly shift towards higher/lower potentials, which is caused by electrode polarization. Moreover, the CV profile maintains its shape even at higher scan rates, indicating the excellent reversibility of the Ru@N-doped C-modified electrode. The specific capacitance (Cs) of Ru@N-doped C has been calculated from the respective integral areas of each CV profile at varying scan rates using Equation S(1). As can be seen in Fig. 5(c), the Cs value is slightly reduced upon increasing the potential scan rate from 10 mV s^{-1} to 100 mV s^{-1}. An observation of lower Cs at a higher scan rate is due to the insufficient time for electrolyte ions to reach the active sites of the electrode materials. However, more than 75 % of the initial Cs (280 F g^{-1} @ 5 mV s^{-1}) has been retained at the higher scan rate of 100 mV s^{-1} (200 F g^{-1}). This excellent rate capability is achieved through structural stability through doping of a heteroatom, resulting in the coexistence of graphitic and amorphous carbons, which retains the conductivity of Ru, and thus, specific capacitance has been retained even at higher scan rates [44]. Moreover, to study the type of energy storage mechanism involved in Ru@N-doped C-based electrode was analyzed through the peak current (ip) and scan rate (ν), using the following power-law relation: $i_p = a\nu^b$ (with a and b as adjustable parameters). Based on the theoretical predictions, if the slope (b-value) is 1, it indicates a surface capacitive-controlled process, and 0.5 means a diffusion-controlled process [45]. A linear relationship was obtained by adopting double logarithmic plot between peak current (ip) and scan rate (ν) at a fixed potential and the resultant slope (b-value) is calculated to be 0.93 (anodic current) and 0.88 (cathodic current), indicates that electrochemical process involved at Ru@N-doped C is dominated by capacitive controlled process [Fig. 5(d)]. As can be seen from the CV curve, the Ru@N-doped C electrode is involved with pseudocapacitive (due to the presence of Ru) and EDLC process (due to the presence of N-doped graphitic C), without any observation of water oxidation within the applied potential region. As a wider potential range (up to 1.0 V) was involved at Ru@N-doped C electrodes, the electrochemical mechanism at each potential value was also studied by adopting a power law relation. As illustrated in Fig. 5(e) and (f), the b-values of both the anodic and cathodic regions of Ru@N-doped C electrode are in the range between 0.9 and 1.0, indicating a capacitive-controlled process is dominated within the potential range from 0.2 to 0.8 V. This process has been validated using Randle's Sevick equation and a linear plot was observed between redox peak responses *vs* various scan rates [Fig. 5(g)]; R^2 = 0.997 (cathodic) and R^2 = 0.998 (anodic)), confirming that the Ru@N-doped C electrode facilitates the pseudocapacitive behavior. To further quantify the capacitive contribution of Ru@N-doped C electrode by adopting the Duun model as explained in the following expression, $i(V) = k_1\nu + k_2\nu^{1/2}$. By plotting a calibration plot between $\nu^{1/2}$ and $i(V)/\nu^{1/2}$, the values of $k_1\nu$ and $k_2\nu^{1/2}$ are calculated from the slope and intercept of the linear regression [46–50]. By adopting the Dunn model at 10 mV s^{-1}, the CV response for Ru@N-doped C electrode is dominated by capacitive contribution (74.1 %) along with diffusion contribution of about 25.9 %, respectively, as represented in Fig. 5(h). Further to extend the capacitive contribution for the Ru@N-doped C electrode was calculated at various scan rates. It can be observed that the ratio of capacitive-controlled contribution gradually increased from 74.1 % to 90.1 % with increasing scan rates (10 mV s^{-1} to 100 mV s^{-1}), highlighting that the pseudocapacitive process is dominated at Ru@N-doped C electrode [Fig. 5(i)]. The higher capacitive contribution at lower scan rates might be due to the rapid redox process involved at Ru^{3+}/Ru^{2+} in 1 M H_2SO_4 facilitates shorter diffusion pathways through the large surface area offered by metallic Ru and N-doped C formed at the heterointerface.

The electrochemical behavior of the fabricated Ru@N-doped C electrode was further evaluated using GCD measurements at 1–10 A g^{-1}. As illustrated in Fig. 6(a), the GCD profiles exhibit a nearly symmetric response with non-linear (pseudo) behavior with minimal or negligible voltage drop (iR) at the onset of the discharge curve. Notably, the GCD profile shape is well-maintained even at higher current densities, indicating the electrode's ability to facilitate rapid charge-discharge processes accompanied by reversible redox reactions. Furthermore, the GCD results closely align with Fig. 5(a), reinforcing the performance of Ru@N-doped C electrode in 1 M H_2SO_4. The specific capacitance (Cs) of the Ru@N-doped C electrode was found to be inversely proportional to both the scan rate and the applied GCD current density. The Cs values calculated from the equation [Eq. S(2)] at different current densities are calculated to be 211.1, 176.7, 152.3, 144.5, and 136.8 for 1, 3, 5, 7, and 10 A g^{-1}, respectively [Fig. 6(b)], demonstrating a capacitance retention of 64.8 %, highlighting the electrode's good rate capability. Moreover, long-term cyclic stability and durability of Ru@N-doped C-modified electrode were assessed at constant current density (10 A g^{-1}), as shown in Fig. 6(c). The electrode retained approximately 93.8 % of its initial capacitance value after 5000 continuous GCD cycles at 10 A g^{-1}, indicating excellent cycling durability. In addition, the coulombic efficiency remained as high as ~98 % under the same conditions, demonstrating superior reversibility and electrochemical feasibility. To evaluate the changes of the positive electrode before and after cycles, Electrochemical impedance spectroscopy (EIS) was employed [Fig. S4(b)]. Interestingly, the EIS performance for Ru@N-doped C after being

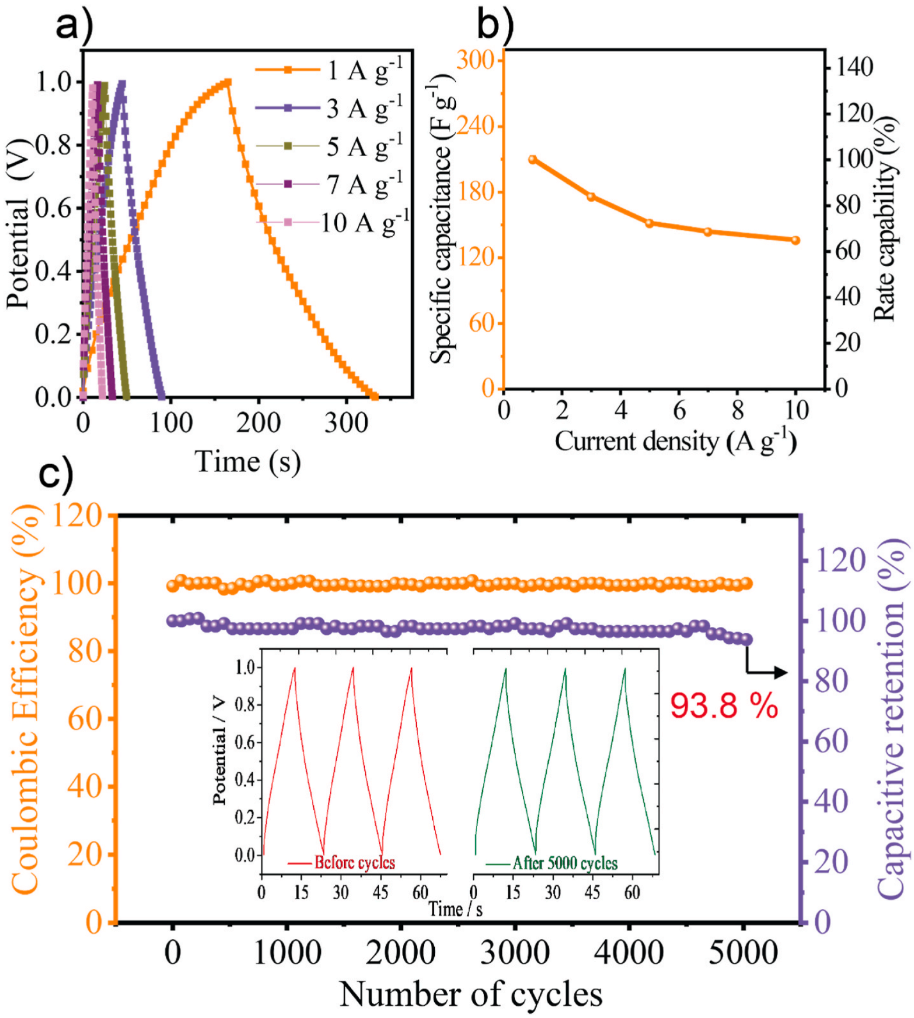

Fig. 6. (a) GCD plots of Ru@N-doped C at different current densities. (b) The specific capacitance of Ru@N doped C from the GCD plots at different current densities. (c) The columbic efficiency and capacitive retention of Ru@N-doped C at a current density of 10 A g^{-1} (Inset) GCD curves before and after 5000 cycles.

subjected to cyclic stability for 5000 cycles experiences a decrease in R_{ct} value (~1 Ω) when compared with EIS data before cycles, which suggests enhanced charge transfer characteristics and confirms the structural robustness of the Ru@N-doped C electrode. The analytical parameters, such as potential window (V), specific capacitance obtained from scan rate and current densities for Ru@N-doped C are found to be good and compared with other previously reported RuO_2-based electrodes that existed in the literature (Table S1).

Interestingly, the obtained retention value was found to be higher than other previously reported electrodes, which might be due to the formation of a nano-heterointerface layer (N-doped C) around metallic Ru, facilitating good conductivity through a fast redox-active electrochemical process. When compared with RuO_2, Ru@N-doped C in the presence of electrolyte utilizes predominant Ru electroactive sites that exist in porous carbon matrix and does not favor agglomeration (as evident from Fig. 4(a)). The porous nanostructure of Ru@N-doped C offers a facile ion transport pathway for a fast charge transfer process and thus results in high capacitance retention (93.8 %) with high efficiency (98 %) even after 5000 cycles. In addition, the presence of N dopant exhibited excellent electrical conductivity, which favors reversible charging/discharging, and signifies the involvement of a faradaic reaction leading to enhanced pseudocapacitance. The electrochemical stability of the Ru@N-doped C electrode was comparatively high because of minimal degradation of material over continuous charge/discharge cycles in accordance with Fig. 6(c) Inset.

To better understand the structural and morphological analysis of the Ru@N-doped C electrode before and after cycling was conducted. Initially, ex-situ XRD analysis was carried out to investigate the structural changes. Fig. S4(a) compares the XRD pattern for Ru@N-doped C electrode before and after 5000 cycles recorded in the presence of 1 M H_2SO_4 at a current density of 10 A/g. It can be seen from Fig. S4(a) that the observation of strong diffraction peaks corresponds to graphitic carbon, indicating the presence of graphite foil as a current collector. The enlarged view shows the observation of diffraction peaks located at 37.98, 44.11, 59.40, 69.60, and 77.64, which are well-matched with the metallic Ru in accordance with ICDD card No. 002–1258. Interestingly, after being subjected to cycling in the presence of 1 M H_2SO_4, the diffraction peaks are still maintained with a small decrease in the peak intensity, without any notable shift in the peak value strongly reveals that Ru@N-doped C is not subjected to any structural changes even after 5000 continuous cycles. In addition, the absence of RuO_2 diffraction peaks strongly reveals that N-doped carbon strongly protects the metallic Ru and does not undergo degradation or any phase transformation. This phenomenon is due to its intrinsic pseudocapacitive behavior undergoes surface redox reaction (as revealed from the CV figure), enabling it to store charge either at the electrode/electrolyte interface (N-doped carbon) or within the inner surface.

Additionally, to evaluate the morphological changes of Ru@N-doped C before [Fig. S4(c) and S4(d)] and after cyclic stability [Fig. S4(e) and S4(f)] was evaluated using FESEM analysis. The morphology of the electrode was preserved and retains the layered structure of Ru@N-doped C, along with the presence of conducting carbon as particles (super P) are tightly packed into an interconnected network. However, the electrode obtained after continuous 5000 cycles is free from cracks or any material degradation. The following factors are due to: (i) the presence of metallic Ru provides high conductivity and facilitates rapid charge transfer at the electrode/electrolyte interface, and (ii) the formation of N-doped carbon layers offers rapid accessibility to H_3O^+/SO4^{2-} ions through diffusion of ions through porous channels. These results collectively reveal that synergetic metallic Ru encapsulated by an N-doped C layer protects the material without any structural degradation or morphological changes even after 5000 cycles.

3.3. Characterization of freestanding Ti_3C_2 film

To match the outstanding performance of the Ru@N-doped C positive electrode, a suitable negative electrode is necessary for the design of a high-performance energy storage device. However, the majority of reported negative electrodes are based on carbon materials, which are lacking in specific capacitance due to the absence of a faradaic process in an acidic medium. To overcome the drawbacks of carbon-based negative electrodes, the present work aims to develop a freestanding Ti_3C_2 film that provides well-defined redox peaks in the aforementioned electrolyte, demonstrating the advantages of the Ti_3C_2 film [51,52]. A freestanding Ti_3C_2 film was prepared by previously reported methods, which involve Al etching from Ti_3AlC_2 (MAX) precursor, delamination of multi-layers, and exfoliation of single-layered nanosheets using the LiF/HCl system (MILD method), which can be used as a negative electrode to enhance the specific capacitance [53]. Furthermore, the detailed preparation method for the formation of freestanding Ti_3C_2 film is presented in the experimental part, and the schematic illustration is shown in Fig. S5(a). The prepared freestanding Ti_3C_2 film was characterized by XRD and TEM analysis. The powder XRD patterns in Fig. S5(b) confirm the successful conversion of the Ti_3AlC_2 MAX phase into a freestanding Ti_3C_2 film through selective etching of Al layers and followed by delamination. The diffraction peak corresponding to the (002) plane notably shifted to a smaller angle (2θ from 9.62° to 6.68°), clearly revealing that the Al layer was removed successfully and leading to the formation of freestanding Ti_3C_2 film [54]. In addition, the prominent diffraction peak at 38.92° (104) in the Ti_3AlC_2 phase significantly diminished in the freestanding Ti_3C_2 film, further indicating the transformation of MAX phase into the MXene structure [55,56]. Moreover, the TEM image of the prepared freestanding Ti_3C_2 film confirms a single-layered two-dimensional structure [Fig. S5(c)]. The formation of the single-layered wrinkled structure is greatly facilitated by Li^+ ion intercalation during the delamination process, promoting extensive

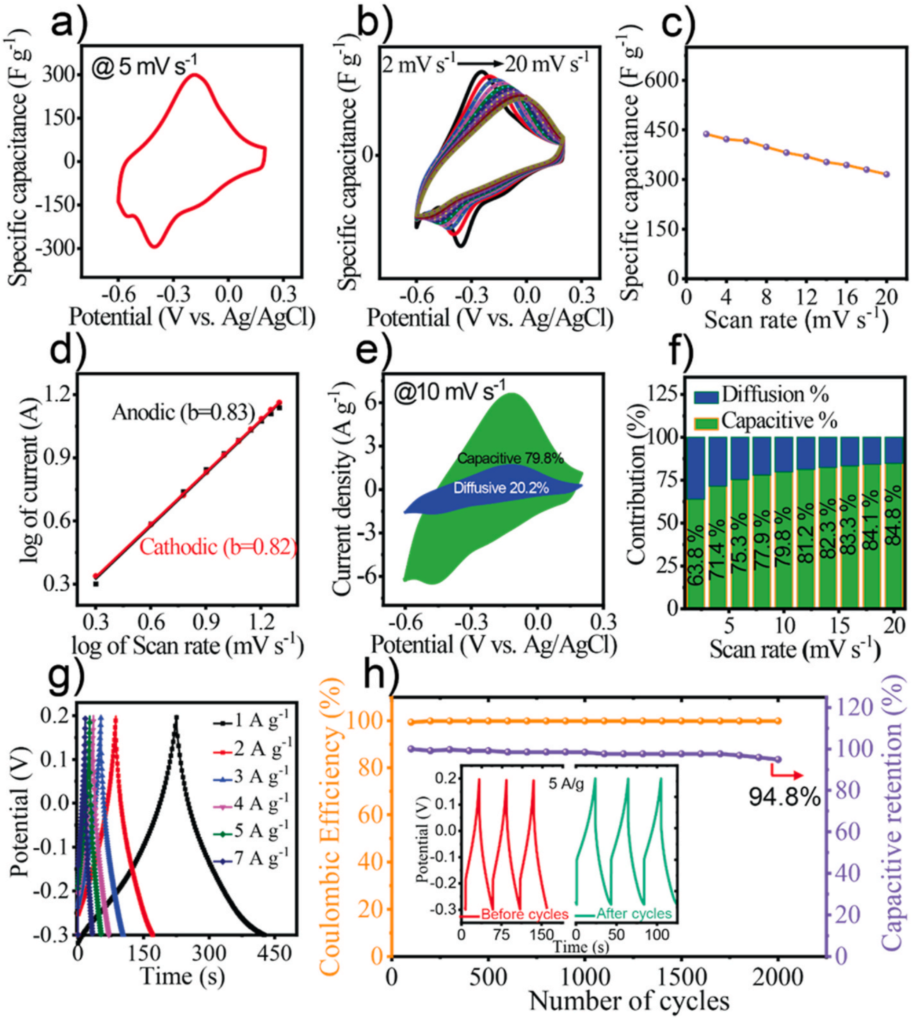

Fig. 7. Electrochemical performance for the freestanding Ti_3C_2 film negative electrode. (a) The CV response for freestanding Ti_3C_2 film electrode in 1 M H_2SO_4, at 5 mV s^{-1} using three electrode cell configuration (b) CV curves of freestanding Ti_3C_2 film electrodes at different scan rates. (c) The specific capacitance of freestanding Ti_3C_2 film obtained from various scan rates. (d) Log current vs log scan rate of freestanding Ti_3C_2 film. (e) Capacitive and diffusive contributions obtained at 10 mV s^{-1}. (f) Contribution of capacitive and diffusive-controlled processes at different scan rates.

exfoliation, and the resultant material was collected in a storage bottle. The photograph of the freestanding Ti_3C_2 film obtained via vacuum filtration is displayed in Fig. S5(d).

3.4. Electrochemical characterization of freestanding Ti_3C_2 film as negative electrode

To exhibit pseudocapacitive behavior as a negative electrode, the processing of MXene solution into a freestanding Ti_3C_2 film facilitates the intercalation of H_2O molecules between the stacked layers, thereby activating the redox capability of Ti–O bonds [57,58]. This results in a pseudocapacitive charge storage mechanism in an acidic medium. The electrochemical energy storage performance of the freestanding Ti_3C_2 film was evaluated in 1 M H_2SO_4 using a three-electrode electrochemical cell configuration. As shown in Fig. 7(a), the freestanding Ti_3C_2 film displays well-resolved redox peaks located at $E_{pa} = -0.18$ V and $E_{pc} = -0.39$ V versus Ag/AgCl within the potential range of 0.2 to −0.6 V at a scan rate of 5 mV s^{-1}, representing a highly reversible pseudocapacitive charge storage process. The observation of redox behavior in the Ti_3C_2 film is consistent with previously reported MXene film-based electrodes, further confirming the successful formation of a freestanding Ti_3C_2 film, which can act as a current collector [29]. To investigate charge storage kinetics and assess the retention of redox peaks at varying scan rates, CV measurements were performed over a scan rate range of 2–20 mV s^{-1} [Fig. 7(b)]. The well-defined anodic and cathodic peaks were consistently observed in both anodic and cathodic scans, with an increasing scan rate of 20 mV s^{-1}. Furthermore, the anodic and cathodic peak potentials shifted positively and negatively, respectively, indicating rapid and reversible surface redox reactions involving intercalated protons and terminal oxygen-containing functional groups (−OH and =O) on the Ti_3C_2 surface. By applying the power law relationship, the *b*-value derived from the slope provides important insight into the nature of the charge storage mechanism. For the Ti_3C_2 film as a negative electrode, the *b*-value was calculated to be 0.83 and 0.82 (approximately ~1) for both anodic and cathodic processes, suggesting the electrochemical process is involved with a capacitive charge storage mechanism [Fig. 7(d)] [59]. The Cs of the freestanding Ti_3C_2 film were calculated using Equation S(1), based on the integral area of CV profiles across different scan rates. In addition, Fig. S6 shows a strong linear relationship between redox peak currents and the scan rates (Randles–Sevcik plots), with $R^2 = 0.997$ (cathodic) and $R^2 = 0.998$ (anodic), further confirming the pseudocapacitive behavior of the freestanding Ti_3C_2 film. As depicted in Fig. 7(c), the Cs value gradually decreased with an increasing scan rate from 2 to 20 mV s^{-1}, yet retained 72.13 % of its original capacitance of 315.6 F g^{-1} @ 20 mV s^{-1} compared to 437.5 F g^{-1} @ 2 mV s^{-1}. The capacitive contribution of the Ti_3C_2 film was also evaluated using Dunn's equation, and the capacitive contribution at a scan rate of 10 mV s^{-1} was calculated to be 79.8 %, [Fig. 7(e)], indicating a surface-controlled charge storage process at the Ti_3C_2 film electrode.

Furthermore, the overall capacitive and diffusion-controlled contributions were evaluated across the full scan rate range. As the scan rate increased from 2 to 20 mV s^{-1}, surface capacitance contribution also increased from 63.8 % to 84.8 %, while the diffusion-controlled contribution decreased from 36 % to 15 % [Fig. 7(f)]. In conclusion, the freestanding Ti_3C_2 film can act as a pseudocapacitive electrode material. As scan rates increase, the contribution from diffusion-controlled processes diminishes due to the limited efficiency of electrolyte ion insertion into the MXene crystal lattice, thus enhancing the surface-controlled capacitive performance [60]. The GCD profiles of the freestanding Ti_3C_2 film, evaluated as a negative electrode at various current densities from 1 to 7 A g^{-1}, display symmetric shapes with a minimal iR drop, indicating pseudocapacitive charge storage behavior [Fig. 7(g)]. Based on the GCD data, the Cs of the freestanding Ti_3C_2 film reach 266 F g^{-1} @ 1 A g^{-1} and retain 147 F g^{-1} when the current density is increased tenfold to 10 A g^{-1} [Fig. S7(a)], demonstrating good rate capability. In addition, cyclic stability and durability were assessed by subjecting the freestanding Ti_3C_2 film negative electrode to 2000 continuous GCD cycles at a current density of 5 A g^{-1}. The results, shown in Fig. 7(h), reveal that the electrode retained 94.8 % of its initial capacitance along with a high coulombic efficiency of 99.8 %. Fig. 7(h) inset further highlights that the GCD profile exhibited similar response in charging and discharging times even after being subjected to 2000 continuous cycles, which can be attributed to the robust redox activity and stable capacitive characteristics of the freestanding Ti_3C_2 film. To further understand the ion transport and charge transfer properties of the freestanding Ti_3C_2 film electrode, electrochemical impedance spectroscopy (EIS) measurements were conducted. Fig. S7(b) presents a comparison of Nyquist plots obtained before and after 2000 continuous GCD cycles. The negligible change in resistance observed indicates excellent structural and electrochemical stability of the material during long-term cycling.

3.5. Asymmetric supercapacitor device

Thanks to the excellent pseudocapacitive electrochemical performance of the Ru@N-doped C and freestanding Ti_3C_2 film, they were employed as active electrodes to construct an all-pseudocapacitive ASC device, denoted as freestanding Ti_3C_2 film//Ru@N-doped C, which is separated by glass-microfiber as a separator. The electrochemical characterization was conducted in a two-electrode configuration (full-cell) where Ru@N-doped C was coated on graphite foil, as the positive electrode, while the freestanding Ti_3C_2 film, placed on graphite foil was functioned as the negative electrode. A Glass microfiber-GF/D separator was used between the electrodes to assemble a split-cell ASC device. Fig. 8(a) displays a schematic cell assembly of the fabricated ASC. Fig. 8 (b) presents CV curves of the individual electrodes Ru@N-doped C (0–1.0 V), freestanding Ti_3C_2 film (0.2 to −0.6 V), which together combine to provide an overall cell potential of 1.5 V, all measured at a scan rate of 10 mV s^{-1}. The asymmetric device exhibits well-defined, reversible redox peaks within its potential window (1.5 V), which are in closer agreement with the pseudocapacitive behavior of both positive and negative components, without any observation of oxygen evolution reaction. Fig. 8(c) represents CV curves of freestanding Ti_3C_2 film//Ru@N-doped C as an ASC device recorded at increasing scan rates from 10 to 100 mV s^{-1}. All the CV curves obtained from various scan rates display distinct and reversible redox peaks, indicating that both positive and negative electrodes possess good wettability with facile ion-diffusion pathways across the separator, which can retain pseudocapacitive behavior. To evaluate the operating voltage of the fabricated ASC device, GCD measurements of the ASC at varying operating voltages (1.0–1.6 V) as represented in Fig. 8(d). The device maintained stable performance without significant polarization up to 1.5 V at a current density of 5 A g^{-1}.

Beyond this voltage, a large plateau appeared, indicating the onset of electrolyte decomposition or side reactions. Therefore, 1.5 V was fixed as the optimized working potential window for further electrochemical testing. Fig. 8(e) displays the GCD profiles of the freestanding Ti_3C_2//Ru@N-doped C device at various current densities (1 A g^{-1} to 30 A g^{-1}) and exhibits nearly symmetrical charge–discharge curves without any observation of iR drop, signifying the operating ability of the device even at higher current densities. The Cs, calculated from the GCD curves, are 194.3, 189.8, 182.5, 169.0, 156.2, 138.3, 133.3, and 120.0 F g^{-1} at current densities of 1, 2, 3, 5, 7, 10, 20, and 30 A g^{-1}, respectively [Fig. S8]. These results highlight the excellent rate capability of the ASC, maintaining substantial capacitance even at a higher current density of 30 A g^{-1}. Fig. 8(f) presents a comparative analysis (Ragone plot) between energy and power density for the fabricated ASC device and other reported systems. Based on the equation adopted using power and energy density as provided in (Eq. SI [5and6]), the resultant freestanding Ti_3C_2//Ru@N-doped C ASC device delivers a high energy density of 60.7 Wh kg^{-1} and power density of 1294 W kg^{-1}, underscoring the

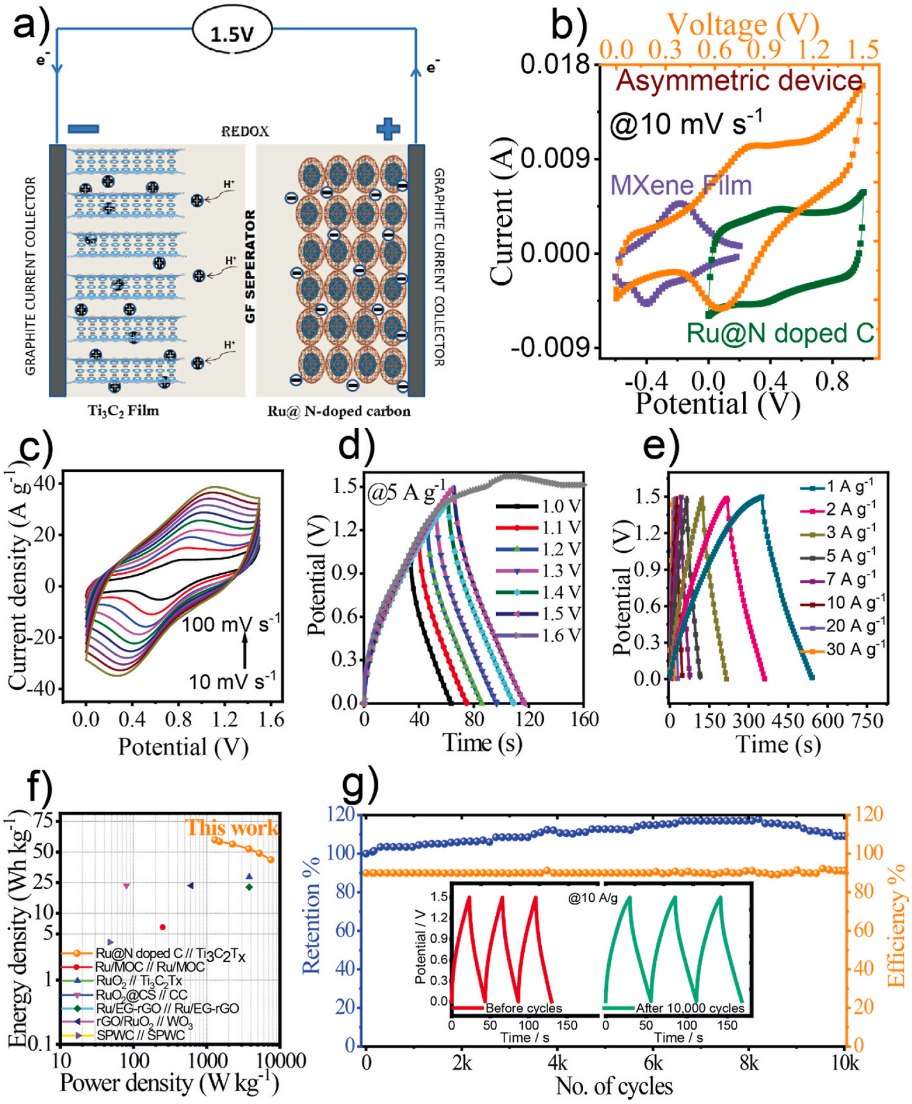

Fig. 8. (a) Schematic illustration of the as-fabricated asymmetric supercapacitor device based on Ru@N doped C as the positive electrode and a freestanding Ti_3C_2 film as the negative electrode. (b) CV profiles of Ru@N-doped C, freestanding Ti_3C_2 film, and freestanding Ti_3C_2 film//Ru@N-doped C ASC device at a scan rate of 10 mV s^{-1}. (c) CVs of Ti_3C_2 film//Ru@N-doped C ASC device at different scan rates. (d) GCD profiles of Ti_3C_2 film//Ru@N-doped C at different potentials. (e) GCD profiles of Ti_3C_2 film//Ru@N-doped C ASC at different current densities. (f) Ragone plot for various reported Ru-based devices. (g) The columbic efficiency and capacitive retention of Ti_3C_2 film//Ru@N-doped C ASC device at a current density of 10 A g^{-1}, (Inset) GCD plots of Ti_3C_2 film//Ru@N-doped C ASC device before and after 10000 cycles at 10 A g^{-1}.

advantages of employing pseudocapacitive materials as both positive and negative electrodes [Table S2]. The performance of freestanding Ti_3C_2//Ru@N-doped C ASC device (60.7 Wh kg^{-1} and 1294 W kg^{-1}) was compared in terms of energy density (Wh kg^{-1}) and power density (W kg^{-1}) with previously reported electrodes namely Ru/MOC//Ru/MOC (6.3 Wh kg^{-1} and 250 W kg^{-1}) [61], $Ti_3C_2T_x$//RuO_2 (29 Wh kg^{-1} and 3800 W kg^{-1}) [31], AC//RuO_2@CS (23.1 Wh kg^{-1} and 80 W kg^{-1}) [62], Ru/EG-rGO//Ru/EG-rGO (22.1 Wh kg^{-1} and 3800 W kg^{-1}) [63], WO_3//rGO/RuO_2 (23 Wh kg^{-1} and 613 W kg^{-1}) [64], and SPWC//SPWC (3.765 Wh kg^{-1} and 47.5 W kg^{-1}) [24], Based on the previously reported works, the present work highlights an enhancement in the energy density and power density when compared with other previously reported RuO_2-based electrodes, which might be due to the involvement of all pseudocapacitive electrodes in energy storage devices. Alshareef et al. [31] fabricated a pseudocapacitive Ti_3C_2//RuO_2 asymmetric supercapacitor to improve energy density and overcome the limited capacitance of traditional carbon-based materials using a pseudocapacitive charge storage mechanism of both positive and negative electrodes. As fabricated Ti_3C_2//RuO_2 asymmetric device also shows good performance for long-term application, with synergistic contribution from all pseudocapacitive charge storage mechanisms of RuO_2 and Ti_3C_2, and reaches a maximum potential window of 1.5 V in aqueous 1M H_2SO_4. The assembled device shows excellent rate capability even at a high scan rate of 1000 mV s^{-1} due to the high electrical conductivity of RuO_2 and Ti_3C_2. Although, Ti_3C_2//RuO_2 device has shown better performance than traditional carbon-based asymmetric supercapacitors, it can't meet the high energy application due to the low specific energy of 29 Wh/kg. Comparatively, the proposed asymmetric device fabricated based on Ti_3C_2//Ru@N-doped C shows enhanced charge/discharge time due to the presence of N dopant will provide more redox active sites for faradaic reaction with improved pseudocapacitive charge storage kinetics, and high surface area offered by graphitic porous carbon provides abundant sites for electrolyte ions to penetrate it, resulting in improvement of overall performance. Due to the synergistic contribution of N-doped C (electroactive) with efficient utilization of Ru metal in the matrix, and thus the fabricated asymmetric device Ti_3C_2//Ru@N-doped C reached a high energy density of 60.7 Wh/kg, which was comparatively higher than RuO_2//Ti_3C_2 for long-term energy applications.

To evaluate the practical applicability of the device, long-term cyclic stability and durability were assessed over 10,000 continuous GCD cycles recorded at 10 A g^{-1}, as shown in [Fig. 8(g)]. Impressively, the device exhibited a gradual increase in capacitance retention, reaching approximately 112 % after 3750 cycles. Further increase in cyclic stability, a slight decrease in capacitive retention and followed by a gradual increase in capacitive retention, and reached 117 % after 6600 cycles. With extended cycling, the capacitive retention reached 109 % after 10,000 cycles [Fig. 8(g) Inset]. To evaluate the changes in the electrode material after being subjected to continuous 10,000 cycles, EIS analysis was carried out [Fig. S9]. Based on the EIS response, there is no significant change in the Rct value, revealing that the electrode material did not undergo any changes, indicating the cyclic ability of the fabricated ASC device. Additionally, all pseudocapacitive ASC devices consistently demonstrated high coulombic efficiency, maintaining nearly 92 % throughout the entire cycling test [Fig. 8(g)]. These outstanding energy storage characteristics highlight the potential of the freestanding Ti_3C_2//Ru@N-doped C device for future commercial energy storage applications.

3.6. Post-mortem analysis

To evaluate the structural and morphological changes after cyclic stability of 10,000 continuous cycles, the fabricated Ti_3C_2 film//Ru@N-doped C device was dismantled and subjected to XRD and FESEM analysis. Initially, XRD analysis was carried out for Ru@N-doped C electrode before and after 10,000 cycles [Fig. S10(a)]. The observation of stronger diffraction peaks corresponds to the graphitic carbon, revealing the successful coating of active electrode material on the current collector surface. When compared with before cycles, the diffraction peaks correspond to after 10,000 cycles exhibited diffraction peaks (38.3°, 43.9°, 58.8°), which are found to be similar without any significant change in the peak value. The resultant diffraction peak values are in well-accordance with metallic Ru (002-1258- ICDD). Therefore, this provides clear evidence for the existence of metallic Ru, which is well protected by an N-doped C layer, and did not allow any structural changes when subjected to continuous cycles from an asymmetric device.

In addition, to investigate the morphological changes of the positive electrode (Ru@N-doped C) from the asymmetric device were investigated using FESEM analysis. The morphological investigation of Ru@N-doped C before [Fig. S10(b) and S10(c)] and after being subjected to continuous 10,000 cycles [Fig. S10(d) and S10(e)]. As revealed from the backscattered FESEM image, the existence of clear and brighter spots corresponds to the existence of metallic Ru (heavier element) and is found to be comparable with the darker region of carbon (light element). The distinguishable region of brighter spots clearly evidences that metallic Ru did not undergo any morphological changes after 10,000 cycles. To evaluate the presence of electrolyte ions, present in Ru@N-doped C, EDAX and mapping analysis were carried out. Fig. S10(g–h) evidence that the resultant Ru@N-doped C electrode is composed of Ru, C, N, S, and O. This feature strongly reveals that during the charging and discharging process, the SO_4^{2-} electrolyte ions are involved mainly in ionic diffusion. Due to the wettability of electrolyte from the outer surface along with activation of electroactive species, a gradual increase in the capacitive retention was observed from the first cycle and reached 112 % after 3750 cycles (stage 1). This phenomenon signifies the ion diffusion of SO_4^{2-} from the outer layer and reaching the middle layer through porous channels exhibited in Ru@N-doped C (as revealed from Fig. 3(c)). Further increase in cyclic stability, a slight decrease in capacitive retention and followed by a gradual increase in capacitive retention, and reached 117 % after 6600 cycles (stage 2). This further evidence the wettability and activation of electroactive species via ionic diffusion of SO_4^{2-} from the middle layer and reached the central canal of the electrode. After complete wettability of the electrode, the capacitive retention reached 109 % after 10,000 cycles. The primary reasons for the increase in retention of the electrode might be due to an increase in electroactive sites that participate in redox reaction, activation of material through complete wettability of the electrode after continuous charge-discharge process, which favors mass diffusion of electrolyte ions to reach the deep channels or voids within the electrode.

4. Conclusions

In summary, we first reported the transformation of pillared non-conductive Ru-MOF into Ru@N-doped carbon layer via thermal annealing process using melamine as nitrogen source. The unique architecture of the metallic Ru layer surrounded by N-doped graphitic carbon at the nano heterointerface layer provides abundant redox-active sites and efficient transport pathways, resulting in a high specific capacitance (211.1 F g^{-1}), excellent rate capability (64.8 %), and superior retention (93.8 %) and good faradaic efficiency (98 %) for continuous 5000 cycling stability. The resultant Ru@N-doped C as a positive electrode was successfully fabricated with MXene free-standing Ti_3C_2 film as a negative electrode as the asymmetric device. The fabricated all-pseudocapacitive-based positive and negative electrodes delivered a superior energy density of 60.7 Wh kg^{-1} than the previously reported RuO_2-based asymmetric device with a power density of 1294 W kg^{-1}. Therefore, the present work highlights the role of fabricating all pseudocapacitive electrodes as an asymmetric device, which guides a new pathway for researchers working on designing electrodes in supercapacitors. Therefore, in conclusion, the fabrication of all pseudocapacitive electrodes will be an alternative to conventional devices, which could hold a strong place in wearable or flexible devices where high energy density is required.

CRediT authorship contribution statement

Elangovan Sivasurya: Writing – original draft, Formal analysis, Data curation, Conceptualization. **Mari Elancheziyan:** Formal analysis, Data curation, Conceptualization. **Francis Ashamary:** Formal analysis, Data curation, Conceptualization. **Ganesan Maheswari:** Formal analysis, Data curation, Conceptualization. **Atchudan Raji:** Data curation, Conceptualization. **Mohamed Gamal Mohamed:** Writing – review & editing, Writing – original draft, Supervision, Investigation, Formal analysis, Data curation, Conceptualization. **Annamalai Padmanaban:** Data curation, Conceptualization. **Keehoon Won:** Supervision. **Pramod K. Kalambate:** Writing – original draft, Supervision. **Shiao-Wei Kuo:** Supervision. **Devaraj Manoj:** Writing – review & editing, Writing – original draft, Supervision, Resources.

Declaration of competing interest

The authors declare that they have no known competing financial interests or personal relationships that could have appeared to influence the work reported in this paper.

Acknowledgements

This study was supported financially by the National Science and Technology Council, Taiwan, under contracts NSTC 112-2223-E-110-002- and 112-2218-E-110-007.

Appendix A. Supplementary data

Supplementary data to this article can be found online at https://doi.org/10.1016/j.jpowsour.2025.238813.

Data availability

Data will be made available on request.

References

[1] Y. Zhu, S. Murali, M.D. Stoller, K.J. Ganesh, W. Cai, P.J. Ferreira, A. Pirkle, R. M. Wallace, K.A. Cychosz, M. Thommes, D. Su, E.A. Stach, R.S. Ruoff, Carbon-based supercapacitors produced by activation of graphene, Science 332 (2011) 1537–1541, https://doi.org/10.1126/science.1200770.

[2] M.G. Mohamed, S.Y. Chang, M. Ejaz, M.M. Samy, A.O. Mousa, S.W. Kuo, Design and synthesis of bisulfone-linked two-dimensional conjugated microporous polymers for CO_2 adsorption and energy storage, Molecules 28 (2023) 3234, https://doi.org/10.3390/molecules28073234.

[3] M.M. Samy, M.G. Mohamed, S.U. Sharma, S.V. Chaganti, T.H. Mansoure, J.T. Lee, T. Chen, S.W. Kuo, Constructing conjugated microporous polymers containing triphenylamine moieties for high-performance capacitive energy storage, Polymer 264 (2023) 125541, https://doi.org/10.1016/j.polymer.2022.125541.

[4] M.G. Mohamed, B. Halder, P.N. Singh, A.A.K. Mohammed, P. Elumalai, S.W. Kuo, Molecular engineering and synergistic redox-active hexaazatrinaphthalene and pyrene-based conjugated microporous polymers for superior faradaic supercapacitor energy storage, Chem. Eng. J. 520 (2025) 165892, https://doi.org/10.1016/j.cej.2025.165892.

[5] M.M. Samy, M.G. Mohamed, S.W. Kuo, Pyrene-functionalized tetraphenylethylene polybenzoxazine for dispersing single-walled carbon nanotubes and energy storage, Compos. Sci. Technol. 199 (2020) 108360, https://doi.org/10.1016/j.compscitech.2020.108360.

[6] M.G. Mohamed, M.G. Kotp, A.O. Mousa, Y.S. Li, S.W. Kuo, Construction of Fe- and N-Doped microporous carbon from ferrocene-based conjugated microporous polymers for supercapacitive energy storage, ACS Appl. Energy Mater. 8 (2025) 2389–2402, https://doi.org/10.1021/acsaem.4c02968.

[7] A. Basit, M.G. Mohamed, S.U. Sharma, S.W. Kuo, Thianthrene- and thianthrene tetraoxide-functionalized conjugated microporous polymers for efficient energy storage, ACS Appl. Polym. Mater. 6 (2024) 12247–12260, https://doi.org/10.1021/acsapm.4c02368.

[8] A. Basit, M.G. Mohamed, M. Ejaz, B.X. Su, H. Manzoor, S.W. Kuo, Boosting supercapacitor energy storage using microporous carbon derived from an octavinylsilsesquioxane and fluorenone-linked porous hybrid polymer, ACS Appl. Energy Mater. 7 (2024) 7505–7516, https://doi.org/10.1021/acsaem.4c01796.

[9] M.M. Samy, M.G. Mohamed, S.U. Sharma, S.V. Chaganti, J.T. Lee, S.W. Kuo, An Ultrastable Tetrabenzonaphthalene-linked conjugated microporous polymer functioning as a high-performance electrode for supercapacitors, J. Taiwan Inst. Chem. Eng. 158 (2024) 104750, https://doi.org/10.1016/j.jtice.2023.104750.

[10] A.O. Mousa, S.U. Sharma, S.V. Chaganti, T.H. Mansoure, P.N. Singh, M. Ejaz, C. H. Chuang, J.T. Lee, S.W. Kuo, Gamal Mohamed Mohamed, Designing strategically functionalized conjugated microporous polymers with pyrene and perylenetetracarboxylic dianhydride moieties with single-walled carbon nanotubes to enhance supercapacitive energy storage efficiency, J. Power Sources 608 (2024) 234624, https://doi.org/10.1016/j.jpowsour.2024.234624.

[11] M.G. Mohamed, C.C. Chen, M. Ibrahim, A.O. Mousa, M.H. Elsayed, Y. Ye, S.W. Kuo, Tetraphenylanthraquinone and Dihydroxybenzene-Tethered conjugated microporous polymer for enhanced CO_2 uptake and supercapacitive energy storage, JACS Au 4 (2024) 3593–3605, https://doi.org/10.1021/jacsau.4c00537.

[12] 4. B.K. Lesel, J.B. Cook, Y. Yan, T.C. Lin, S.H. Tolbert, Using nanoscale domain size to control charge storage kinetics in pseudocapacitive nanoporous $LiMn_2O_4$ powders ACS Energy Lett. 2 (2017) 2293–2298, https://doi.org/10.1021/acsenergylett.7b00634.

[13] J.T. Mefford, W.G. Hardin, S. Dai, K.P. Johnston, K.J. Stevenson, Anion charge storage through oxygen intercalation in $LaMnO_3$ perovskite pseudocapacitor electrodes, Nat. Mater. 13 (2014) 726–732, https://doi.org/10.1038/nmat4000.

[14] H. Ma, B. Zhao, J. Bai, P. Wang, W. Li, Y. Mao, X. Zhu, Z. Sheng, X. Zhu, Y. Sun, Crystallinity tuning of $Na_3V_2(PO_4)_3$: unlocking sodium storage capacity and inducing pseudocapacitance behavior, Adv. Sci. 10 (2023) 2203552, https://doi.org/10.1002/advs.202203552.

[15] A. Ghosh, E.J. Ra, M. Jin, H. Jeong, T.H. Kim, C. Biswas, Y.H. Lee, High pseudocapacitance from ultrathin V_2O_5 films electrodeposited on self-standing carbon-Nanofiber paper, Adv. Funct. Mater. 21 (2011) 2541–2547, https://doi.org/10.1002/adfm.201002603.

[16] S. Korkmaz, İ.A. Kariper, O. Karaman, C. Karaman, The production of rGO/RuO_2 aerogel supercapacitor and analysis of its electrochemical performances, Ceram. Int. 47 (2021) 34514–34520, https://doi.org/10.1016/j.ceramint.2021.08.366.

[17] C. Choi, D.S. Ashby, D.M. Butts, R.H. DeBlock, Q. Wei, J. Lau, B. Dunn, Achieving high energy density and high power density with pseudocapacitive materials, Nat. Rev. Mater. 5 (2020) 5–19, https://doi.org/10.1038/s41578-019-0142-z.

[18] N. Yoshida, Y. Yamada, S. Nishimura, Y. Oba, M. Ohnuma, A. Yamada, Unveiling the origin of unusual pseudocapacitance of $RuO_2 \cdot nH_2O$ from its hierarchical nanostructure by small-angle X-ray scattering, J. Phys. Chem. C 117 (2013) 12003–12009, https://doi.org/10.1021/jp403402k.

[19] P. Zhang, F. Wang, S. Yang, G. Wang, M. Yu, X. Feng, Flexible in-plane micro-supercapacitors: progresses and challenges in fabrication and applications, Energy Store Mater 28 (2020) 160–187, https://doi.org/10.1016/j.ensm.2020.02.029.

[20] A. Morag, N. Maman, N. Froumin, V. Ezersky, K. Rechav, R. Jelinek, Nanostructured nickel/Ruthenium/Ruthenium-Oxide supercapacitor displaying exceptional high frequency response, Adv. Electron. Mater. 6 (2020) 1900844, https://doi.org/10.1002/aelm.201900844.

[21] J. Chu, Z. Liu, J. Yu, H.-G. Wang, F. Cui, G. Zhu, Electronic band structure engineering of π-d conjugated metal-organic framework for sodium organic batteries, Nat. Commun. 16 (2025) 3549, https://doi.org/10.1038/s41467-025-58759-6.

[22] B. Chettiannan, G. Arumugam, S. Mathan, M. Selvaraj, M.A. Assiri, R. Rajendran, Exploring the effect of metal ratio on electrochemical properties of MOF-derived microporous flower-like NiO/Co_3O_4 electrodes for high-performance asymmetric supercapacitor application, J. Energy Storage 119 (2025) 116326, https://doi.org/10.1016/j.est.2025.116326.

[23] T. Mohammadi, M.G. Hosseini, Z. Sadeghi, E. Pastor, K. Wang, Ru/Co metal-organic framework nanosheets arrayed on activated carbon felt as boosted flexible electrodes for symmetric supercapacitors, J. Energy Storage 110 (2025) 115288, https://doi.org/10.1016/j.est.2025.115288.

[24] W. Zhang, S. Yu, H. Hu, Y. Fei, L. Chen, T. Zhang, Binder-free self-supporting electrodes formed by intercalation of RuO_2 on wood-derived carbon for supercapacitor, Appl. Surf. Sci. 640 (2023) 158285, https://doi.org/10.1016/j.apsusc.2023.158285.

[25] M. Islam, MdS. Hossain, B. Adak, M.M. Rahman, K.K. Moni, A.S.M. Nur, H. Hong, H. Younes, S. Mukhopadhyay, Recent advancements in carbon-based composite materials as electrodes for high-performance supercapacitors, J. Energy Storage 107 (2025) 114838, https://doi.org/10.1016/j.est.2024.114838.

[26] V. Strauss, K. Marsh, M.D. Kowal, M. El-Kady, R.B. Kaner, A simple route to porous graphene from carbon nanodots for supercapacitor applications, Adv. Mater. 30 (2018) 1704449, https://doi.org/10.1002/adma.201704449.

[27] A. VahidMohammadi, J. Rosen, Y. Gogotsi, The world of two-dimensional carbides and nitrides (MXenes), Science 372 (2021) eabf1581, https://doi.org/10.1126/science.abf1581.

[28] Z. Ling, C.E. Ren, M.-Q. Zhao, J. Yang, J.M. Giammarco, J. Qiu, M.W. Barsoum, Y. Gogotsi, Flexible and conductive MXene films and nanocomposites with high capacitance, Proc. Natl. Acad. Sci. USA. 111 (2014) 16676–16681, https://doi.org/10.1073/pnas.1414215111.

[29] D. Spurling, H. Krüger, N. Kohlmann, F. Rasch, M.P. Kremer, L. Kienle, R. Adelung, V. Nicolosi, F. Schütt, 3D networked MXene thin films for high performance supercapacitors, Energy Storage Mater. 65 (2024) 103148, https://doi.org/10.1016/j.ensm.2023.103148.

[30] M. Gao, F. Wang, S. Yang, A. Gaetano Ricciardulli, F. Yu, J. Li, J. Sun, R. Wang, Y. Huang, P. Zhang, X. Lu, Engineered 2D MXene-based materials for advanced supercapacitors and micro-supercapacitors, Mater. Today 72 (2024) 318–358, https://doi.org/10.1016/j.mattod.2023.12.009.

[31] Q. Jiang, N. Kurra, M. Alhabeb, Y. Gogotsi, H.N. Alshareef, All pseudocapacitive MXene-RuO_2 asymmetric supercapacitors, Adv. Energy Mater. 8 (2018) 1703043, https://doi.org/10.1002/aenm.201703043.

[32] G. Zhao, W. Guo, M. Shan, Y. Fang, G. Wang, M. Gao, Y. Liu, H. Pan, W. Sun, Metallic ru—ru interaction in ruthenium oxide enabling durable proton exchange membrane water electrolysis, Adv. Mater. 36 (2024) 2404213, https://doi.org/10.1002/adma.202404213.

[33] J. Shen, M. Zhang, Y. Huang, C. Chen, Y. Zheng, S. Dong, J. Jiang, W. Lei, S. Wang, H. Shao, Ru-induced lattice expansion of metallic Co with favorable surface property for high-efficiency water electrolysis, Appl. Catal. B Environ. Energy 358 (2024) 124392, https://doi.org/10.1016/j.apcatb.2024.124392.

[34] B. Zheng, L. Ma, B. Li, D. Chen, X. Li, J. He, J. Xie, M. Robert, T.-C. Lau, pH universal Ru@N-doped carbon catalyst for efficient and fast hydrogen evolution, Catal. Sci. Technol. 10 (2020) 4405–4411, https://doi.org/10.1039/C9CY02552A.

[35] J. Balcerzak, W. Redzynia, J. Tyczkowski, In-situ XPS analysis of oxidized and reduced plasma deposited ruthenium-based thin catalytic films, Appl. Surf. Sci. 426 (2017) 852–855, https://doi.org/10.1016/j.apsusc.2017.07.248.

[36] R. Ma, T. Yang, J. Gao, J. Kou, J.Z. Chen, Y. He, J.T. Miller, D. Li, Composition tuning of Ru-Based phosphide for enhanced propane selective dehydrogenation, ACS Catal. 10 (2020) 10243–10252, https://doi.org/10.1021/acscatal.0c01667.

[37] D.J. Morgan, Resolving ruthenium: XPS studies of common ruthenium materials, Surf. Interface Anal. 47 (2015) 1072–1079, https://doi.org/10.1002/sia.5852.

[38] S. Feng, Y. Zhao, X. Xie, Y. Sun, X. Luo, W. Feng, Unlocking spatial surface energy in porous skeletons: a pathway to bridging electronic circuits from 2D to 3D architectures, Angew. Chem. Int. Ed. 136 (2024) e202412146, https://doi.org/10.1002/ange.202412146.

[39] P. Kurzweil, Precious metal oxides for electrochemical energy converters: pseudocapacitance and pH dependence of redox processes, J. Power Sources 190 (2009) 189–200, https://doi.org/10.1016/j.jpowsour.2008.08.033.

[40] C.-Y. Lee, A.M. Bond, Revelation of multiple underlying RuO_2 redox processes associated with pseudocapacitance and electrocatalysis, Langmuir 26 (2010) 16155–16162, https://doi.org/10.1021/la102495t.

[41] C. Costentin, J.-M. Savéant, Energy storage: pseudocapacitance in prospect, Chem. Sci. 10 (2019) 5656–5666, https://doi.org/10.1039/C9SC01662G.

[42] H.M. Jeong, J.W. Lee, W.H. Shin, Y.J. Choi, H.J. Shin, J.K. Kang, J.W. Choi, Nitrogen-doped graphene for high-performance ultracapacitors and the importance of nitrogen-doped sites at basal planes, Nano Lett. 11 (2011) 2472–2477, https://doi.org/10.1021/nl2009058.

[43] F. Wen, Y. Yan, S. Sun, X. Li, X. He, Q. Meng, J. Zhe Liu, X. Qiu, W. Zhang, Synergistic effect of nitrogen and oxygen dopants in 3D hierarchical porous carbon cathodes for ultra-fast zinc ion hybrid supercapacitors, J. Colloid Interface Sci. 640 (2023) 1029–1039, https://doi.org/10.1016/j.jcis.2023.03.024.

[44] P. Zhang, F. Wang, M. Yu, X. Zhuang, X. Feng, Two-dimensional materials for miniaturized energy storage devices: from individual devices to smart integrated systems, Chem. Soc. Rev. 47 (2018) 7426–7451, https://doi.org/10.1039/C8CS00561C.

[45] Y. Shao, M.F. El-Kady, J. Sun, Y. Li, Q. Zhang, M. Zhu, H. Wang, B. Dunn, R. B. Kaner, Design and mechanisms of asymmetric supercapacitors, Chem. Rev. 118 (2018) 9233–9280, https://doi.org/10.1021/acs.chemrev.8b00252.

[46] M.G. Mohamed, B.X. Su, S.W. Kuo, Robust nitrogen-doped microporous carbon via crown ether-functionalized benzoxazine-linked porous organic polymers for

enhanced CO_2 adsorption and supercapacitor applications, ACS Appl. Mater. Interfaces 16 (2024) 40858–40872, https://doi.org/10.1021/acsami.4c05645.

[47] M.G. Mohamed, M. Ibrahim, N.P. Chen, A. Basit, Y.C. Kao, A.O. Mousa, M. M. Samy, S.W. Kuo, Tetrabenzonaphthalene and redox-active anthraquinone-linked conjugated microporous polymers as organic electrodes for enhanced energy storage efficiency, ACS Appl. Energy Mater. 7 (2024) 5582–5593, https://doi.org/10.1021/acsaem.4c01276.

[48] S.V. Chaganti, S.U. Sharma, M. Ibrahim, A. Basit, P.N. Singh, S.W. Kuo, M. G. Mohamed, Redox-active a pyrene-4,5,9,10-tetraone and thienyltriazine-based conjugated microporous polymers for boosting faradaic supercapacitor energy storage, J. Power Sources 627 (2025) 235848, https://doi.org/10.1016/j.jpowsour.2024.235848.

[49] P. Ghasemiahangarani, G. Farhan, D. Del Mundo, T. Schoetz, Charge storage mechanisms in batteries and capacitors: a perspective of the electrochemical interface, Adv. Energy Mater. 15 (2025) 2404704, https://doi.org/10.1002/aenm.202404704.

[50] N.R. Chodankar, H.D. Pham, A.K. Nanjundan, J.F.S. Fernando, K. Jayaramulu, D. Golberg, Y. Han, D.P. Dubal, True meaning of pseudocapacitors and their performance metrics: asymmetric versus hybrid supercapacitors, Small 16 (2020) 2002806, https://doi.org/10.1002/smll.202002806.

[51] M. Brunet Cabré, D. Spurling, P. Martinuz, M. Longhi, C. Schröder, H. Nolan, V. Nicolosi, P.E. Colavita, K. McKelvey, Isolation of pseudocapacitive surface processes at monolayer MXene flakes reveals delocalized charging mechanism, Nat. Commun. 14 (2023) 374, https://doi.org/10.1038/s41467-023-35950-1.

[52] S. Yang, P. Zhang, F. Wang, A.G. Ricciardulli, M.R. Lohe, P.W.M. Blom, X. Feng, Fluoride-free synthesis of two-dimensional titanium carbide (MXene) using A binary aqueous system, Angew. Chem. Int. Ed. 57 (2018) 15491–15495, https://doi.org/10.1002/anie.201809662.

[53] K. Li, J. Zhao, A. Zhussupbekova, C.E. Shuck, L. Hughes, Y. Dong, S. Barwich, S. Vaesen, I.V. Shvets, M. Möbius, W. Schmitt, Y. Gogotsi, V. Nicolosi, 4D printing of MXene hydrogels for high-efficiency pseudocapacitive energy storage, Nat. Commun. 13 (2022) 6884, https://doi.org/10.1038/s41467-022-34583-0.

[54] H. Shi, P. Zhang, Z. Liu, S. Park, M.R. Lohe, Y. Wu, A. Shaygan Nia, S. Yang, X. Feng, Ambient-stable two-dimensional titanium carbide (MXene) enabled by iodine etching, Angew. Chem. Int. Ed. 60 (2021) 8689–8693, https://doi.org/10.1002/anie.202015627.

[55] J. Zhang, N. Kong, S. Uzun, A. Levitt, S. Seyedin, P.A. Lynch, S. Qin, M. Han, W. Yang, J. Liu, X. Wang, Y. Gogotsi, J.M. Razal, Scalable manufacturing of free-standing, strong $Ti_3C_2T_x$ MXene films with outstanding conductivity, Adv. Mater. 32 (2020) 2001093, https://doi.org/10.1002/adma.202001093.

[56] M. Boota, M. Bécuwe, Y. Gogotsi, Phenothiazine–MXene aqueous asymmetric pseudocapacitors, ACS Appl. Energy Mater. 3 (2020) 3144–3149, https://doi.org/10.1021/acsaem.9b02404.

[57] T. Jiang, Y. Wang, G.Z. Chen, Electrochemistry of titanium carbide MXenes in supercapacitor, Small Methods 7 (2023) 2201724, https://doi.org/10.1002/smtd.202201724.

[58] X. Li, Z. Huang, C.E. Shuck, G. Liang, Y. Gogotsi, C. Zhi, MXene chemistry, electrochemistry and energy storage applications, Nat. Rev. Chem 6 (2022) 389–404, https://doi.org/10.1038/s41570-022-00384-8.

[59] B. Zhang, A. Boretti, S. Castelletto, Mxene pseudocapacitive electrode material for capacitive deionization, Chem. Eng. J. 435 (2022) 134959, https://doi.org/10.1016/j.cej.2022.134959.

[60] S. Bhoi, S.H. Goudar, K.V. Rao, N. Kurra, Extrinsic pseudocapacitance of Ti_3C_2T MXenes in divalent metal-ion electrolytes after assembly with perylene diimides, Cell Rep. Phys. Sci. 5 (2024) 102229, https://doi.org/10.1016/j.xcrp.2024.102229.

[61] B.-S. Lou, P. Veerakumar, S.-M. Chen, V. Veeramani, R. Madhu, S.-B. Liu, Ruthenium nanoparticles decorated curl-like porous carbons for high performance supercapacitors, Sci. Rep. 6 (2016) 19949, https://doi.org/10.1038/srep19949.

[62] R. Zhang, Y. Guo, J. Ning, T. Tao, H. He, F. Guo, Highly dispersed ruthenium oxide nanoparticles on carbon spheres for supercapacitors, Inorg. Chem. Commun. 173 (2025) 113823, https://doi.org/10.1016/j.inoche.2024.113823.

[63] C.-K. Hung, A.R. Thiruppathi, C. McGuire, D.-T. Jiang, A. Chen, Expanded graphite/reduced graphene oxide hybrid architecture functionalized with RuO_2 nanoclusters for high performance energy storage, J. Energy Storage 106 (2025) 114776, https://doi.org/10.1016/j.est.2024.114776.

[64] A.G. Bagde, D.B. Malavekar, A.C. Lokhande, S.D. Khot, C.D. Lokhande, Flexible solid-state asymmetric supercapacitor based on reduced graphene oxide (rGO)/ruthenium oxide (RuO_2) composite electrode, J. Alloys Compd. 980 (2024) 173591, https://doi.org/10.1016/j.jallcom.2024.173591.